INORGANIC CHEMISTRY
FRONTIERS

CHINESE CHEMICAL SOCIETY
ROYAL SOCIETY OF CHEMISTRY

RESEARCH ARTICLE

View Article Online
View Journal | View Issue

Check for updates

Cite this: *Inorg. Chem. Front.*, 2022, **9**, 3559

Mesoporous Mn–Fe oxyhydroxides for oxygen evolution†

Jingyi Han,‡[a] Mingzhu Zhang,‡[b] Xue Bai,[a] Zhiyao Duan,*[b] Tianmi Tang[a] and Jingqi Guan*[a]

Received 5th April 2022,
Accepted 26th May 2022

DOI: 10.1039/d2qi00722c

rsc.li/frontiers-inorganic

The development of high-performance and Earth-abundant catalysts is imperative for the oxygen evolution reaction (OER), and mesoporous oxyhydroxides show huge potential as advanced catalysts toward the OER due to a large specific surface area and porous structure. Here, we adopt a facile template method to synthesize bimetallic Mn–Fe oxyhydroxides. meso-$Mn_1Fe_1O_x$ shows a large BET specific surface area of 212.4 $m^2\ g^{-1}$ and an average pore diameter of 13.1 nm, which favor the exposure of many active sites for the reaction. meso-$Mn_1Fe_1O_x$ exhibits excellent OER performance with a low overpotential of 275 mV at 10 mA cm^{-2}, a small Tafel slope of 52 mV dec^{-1}, and good long-term stability, and is superior to most Mn-based electrocatalysts. Kinetic studies indicate that Fe and Mn sites should synergistically catalyze the OER. Theoretical calculations reveal that the surface doping of Fe onto MnOOH can moderately destabilize the surface bridge O atoms and promote the generation of surface oxygen vacancies that can act as highly active sites for the OER.

Introduction

The oxygen evolution reaction (OER), which is essentially sluggish, plays a crucial role in renewable energy technologies including reversible fuel cells, rechargeable metal/air batteries, and water splitting.[1–6] Ru/Ir-Based materials are the most active OER catalysts in acidic media, but the fancy price and rareness impede their large-scale commercial application.[7,8] So far, a great deal of effort has been made in the fabrication of cost-efficient alternatives, such as transition metal sulfides,[9] selenides,[10] phosphides,[11] borides,[12] carbides,[13] nitrides,[14] oxides/hydroxides/oxyhydroxides,[15] and single-atom catalysts.[16] Among these catalysts, transition metal oxyhydroxides have received much attention due to their higher OER stability than B-, C-, P-, S-, and Se-containing counterparts.[17] Therefore, the development of Earth-abundant and inexpensive transition-metal oxyhydroxides is highly desirable for water splitting application.[18,19] Manganese is the third most abundant transition metal in the crust of the Earth, which has a much lower price than cobalt and nickel.[20] In addition, manganese has excellent redox properties, which make it have good electrocatalytic application potential. However, compared with Ni-, Co-, and Fe-based oxides and hydroxides, Mn-based oxides usually show worse OER performance.[21,22] Therefore, it is alluring and challenging to fabricate high-performance Mn-based catalysts for the OER.[23]

In nature, the oxygen evolution center $CaMn_4O_5$ in photosystem II shows high water oxidation activity with the turnover frequency (TOF) of 100–400 s^{-1}.[24] We found that mononuclear Mn coordinated with four N atoms in graphene exhibited high chemical and electrochemical water oxidation activity with an overpotential (η_{10}) of 337 mV at 10 mA cm^{-2}.[25] Li *et al.* found that γ-MnO_2 showed outstanding OER stability at potentials between 1.6 V and 1.75 V *vs.* RHE in acidic media, but it would be dissolved into the electrolyte at higher potentials due to the formation of MnO_4^-.[26] For unary Mn-based oxides, such as MnO, α-, β-, ε-, δ- and λ-MnO_2, Mn_2O_3, Mn_3O_4, and Mn_5O_8, the electrochemical water oxidation activity is much lower than that of Co-based and Ni-based oxides.[27] Although the OER activity of Mn-based oxides can be significantly enhanced by introducing vacancies and lattice strains, their electrocatalytic performance is still lower than those of Co-based and Ni-based oxides.[28–30]

The Fe-doping strategy is very efficient at improving the OER activity of various transition metal oxides, especially for Co-based and Ni-based oxides.[31,32] Fe doping into transition metal oxide/hydroxide systems can increase the conductivity, improve OER dynamics, adjust redox states and structural transformation of host materials, and modulate the acidity

---

[a] *Institute of Physical Chemistry, College of Chemistry, Jilin University, 2519 Jiefang Road, Changchun 130021, P.R. China. E-mail: guanjq@jlu.edu.cn*
[b] *State Key Laboratory of Solidification Processing, School of Materials Science and Engineering, Northwestern Polytechnical University, Xi'an 710072, P. R. China. E-mail: zhiyao.duan@nwpu.edu.cn*

† Electronic supplementary information (ESI) available: Additional LSV, CV, EIS, TEM, SEM, EDS, and XPS data. See DOI: **https://doi.org/10.1039/d2qi00722c**

‡ These authors contributed equally to this work.

and superexchange interaction, thus enhancing the OER activity. Pan *et al.* found that hollow porous $Mn_{1.2}Fe_{0.8}O_3$ with low crystallinity showed excellent OER activity.[33] Kuang *et al.* fabricated ultrathin low-crystallinity Fe–Mn–O nanosheets onto carbon cloth, which exhibited a low η_{10} of 273 mV for the OER.[34] Li *et al.* supported Mn_3O_4/Fe_2O_3 nanosheets onto nickel foam using an *in situ* hydrothermal method, which demonstrated an ultralow η_{10} of 157 mV for the OER.[35] Lhoste *et al.* found that Mn–Fe-based oxyfluorides can maintain the OER activity at 10 mA cm^{-2} for more than 10 h in 0.5 M H_2SO_4.[36] However, since the strength of the OH–$Mn^{2+\delta}$ is higher than that of the OH–$Fe^{2+\delta}$, resulting in lower OER activity on the Mn sites,[37] the actual active sites of Fe–Mn-based oxides/hydroxides are still not clear because the theoretical overpotentials on Fe or Mn sites are very high.

Herein, we fabricated porous Mn–Fe oxyhydroxides using polyethylene oxide–polypropylene oxide–polyethylene oxide (P123) as the template, which exhibited excellent OER performance, comparable to that of the state-of-the-art IrO_2 catalyst. The Mn/Fe ratio significantly influenced the OER activity and the lowest reaction barrier and the optimal electrocatalytic performance can be achieved on $Mn_1Fe_nO_x$ with Mn/Fe = 1 : 1. Kinetic studies showed that $Mn_1Fe_1O_x$ exhibited a lower energy barrier (32.8 kJ mol^{-1}) than MnO_x (59.6 kJ mol^{-1}) and FeO_x (47.0 kJ mol^{-1}). Theoretical calculations revealed that the surface di-μ-oxo bridged Fe–Mn should be the active site for efficient OER.

Results and discussion

Structure characterization

Mesoporous Mn–Fe hydroxides can be facilely fabricated by a template method using P123 as the template (Fig. 1a). For mesoporous FeO_x, there are three distinct peaks in the XRD pattern, which are centered at 27.4, 36.5, and 47.3°. For mesoporous MnO_x, the main XRD peaks are located at 24.2, 31.5, 41.4, and 51.8°. For meso-$Mn_1Fe_1O_x$, no obvious peaks can be observed, indicating an amorphous structure. For meso-$Mn_1Fe_nO_x$ ($n < 1$), diffraction peaks due to MnO_x can be still observed (Fig. S1†), while for meso-$Mn_1Fe_{1.2}O_x$, there are no obvious diffraction peaks. The meso-$Mn_1Fe_1O_x$ exhibits typical type IV isotherms, indicating a typical mesoporous structure (Fig. 1b). The BET specific surface area of meso-FeO_x, meso-MnO_x, meso-$Mn_1Fe_{0.8}O_x$, meso-$Mn_1Fe_1O_x$ and meso-$Mn_1Fe_{1.2}O_x$ is calculated to be 387.2, 151.1, 256.8, 212.4, and 188.7 m^2 g^{-1}, respectively, and the average pore diameter is 2.2, 13.6, 13.4, 13.1, and 12.8 nm. From the SEM images (Fig. 1c and Fig. S2†) and TEM images (Fig. S3†), irregular nanoparticles are typically observed for meso-FeO_x, meso-MnO_x, and meso-$Mn_1Fe_nO_x$. The HRTEM image (Fig. 1d) and the SAED pattern (Fig. S4†) further indicate no obvious crystalline structure and the existence of mesopores. From the element mapping images, Fe, Mn, and O elements are evenly dispersed in meso-$Mn_1Fe_1O_x$ (Fig. 2 and Fig. S5†). The Fe/Mn ratio in meso-$Mn_1Fe_1O_x$ was determined to be *ca.* 1.05 by

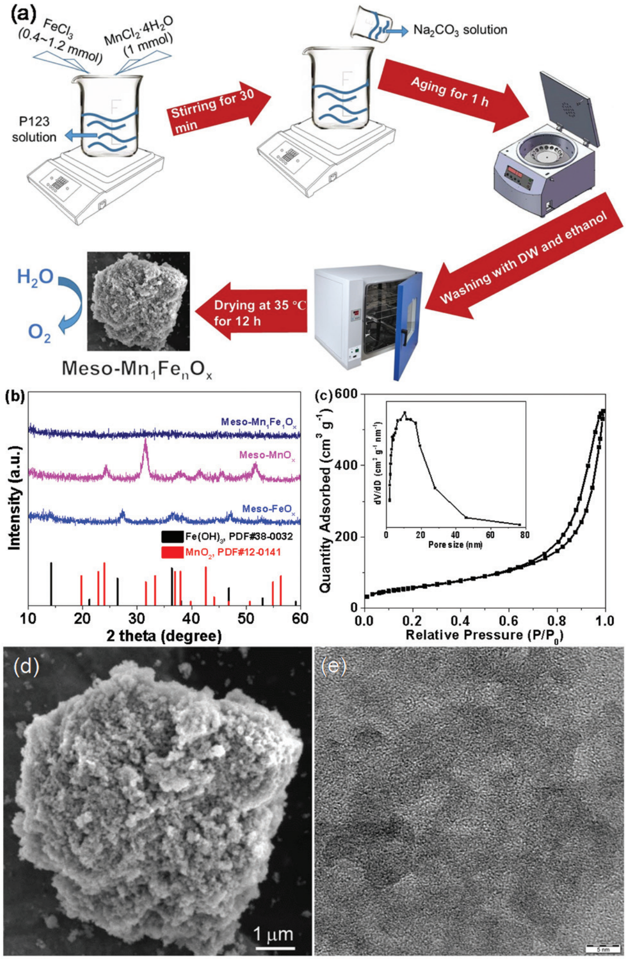

Fig. 1 (a) Synthetic illustration of mesoporous Mn–Fe hydroxides. (b) XRD patterns of meso-FeO_x, meso-MnO_x, meso-$Mn_1Fe_1O_x$, and referred samples. (c) N_2 adsorption–desorption isotherms of meso-$Mn_1Fe_1O_x$ (inset: pore size distribution). (d) SEM image of meso-$Mn_1Fe_1O_x$. (e) HRTEM image of meso-$Mn_1Fe_1O_x$.

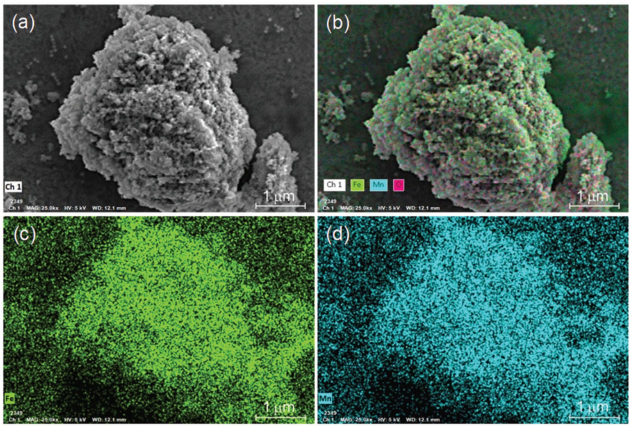

Fig. 2 (a) SEM image of meso-$Mn_1Fe_1O_x$ used for element mapping. (b–d) Element mapping.

SEM-EDS measurement (Fig. S6†) and *ca.* 1.03 by ICP measurement.

The surface composition and metal valence states of meso-$Mn_1Fe_1O_x$ were analyzed by XPS. The XPS survey spectrum reveals the prominent signals of the expected elements, *i.e.*, Fe, Mn, and O (Fig. 3a). The Fe $2p_{3/2}$ spectrum indicates the existence of Fe^{2+} $2p_{3/2}$ and Fe^{3+} $2p_{3/2}$ at 710.9 and 713.1 eV, respectively (Fig. 3b).[38] Moreover, the surface relative content of Fe^{3+}/Fe^{2+} is estimated to be *ca.* 1.2/1. The Mn $2p_{3/2}$ spectrum can be deconvolved into three peaks centered at 640.9, 641.7, and 642.8 eV (Fig. 3c), attributed to Mn^{2+}, Mn^{3+}, and Mn^{4+}, respectively.[39] The O 1s spectrum can be fitted into lattice Fe/Mn–O (529.8 eV) and defective O species (532.5 eV) (Fig. 3d).[40]

OER performance

The OER electrocatalytic properties of meso-$Mn_1Fe_1O_x$, the monometallic counterparts (meso-FeO_x and meso-MnO_x), and IrO_2 were evaluated in 1 M KOH. The meso-$Mn_1Fe_1O_x$ catalyst shows a much lower onset potential and higher current density compared with meso-FeO_x and meso-MnO_x (Fig. 4a), indicating an enhanced intrinsic OER activity due to the synergic effect between Fe and Mn. Specifically, the overpotential (η_{10}) of meso-$Mn_1Fe_1O_x$ at 10 mA cm^{-2} is only 275 mV, which is distinctly lower than that of meso-FeO_x (391 mV) and meso-MnO_x (475 mV), and is comparable to that of IrO_2 (272 mV). The influence of the Fe/Mn ratio on the OER performance was investigated. The results indicate that Fe and Mn with an atomic ratio of 1 : 1 exhibited the best OER performance (Fig. S7†), with a lower η_{10} than that of meso-$Mn_1Fe_{0.4}O_x$ (325 mV), meso-$Mn_1Fe_{0.6}O_x$ (303 mV), meso-$Mn_1Fe_{0.8}O_x$ (289 mV), and meso-$Mn_1Fe_{1.2}O_x$ (356 mV). The Tafel plots in Fig. 4b show that the Tafel slope for meso-$Mn_1Fe_1O_x$ is 52 mV dec^{-1}, smaller than that for meso-FeO_x (106 mV dec^{-1}) and meso-MnO_x (176 mV dec^{-1}) and comparable to that for IrO_2 (55 mV dec^{-1}), indicating high OER efficiency for meso-$Mn_1Fe_1O_x$.[2] The meso-$Mn_1Fe_1O_x$ shows a high turnover frequency (TOF) value of 0.029 s^{-1} per total Fe and Mn atoms and mass activity of 98.6 A g^{-1} at an overpotential of 300 mV, far larger than meso-FeO_x (0.00047 s^{-1} and 1.6 A g^{-1}) and meso-MnO_x (0.00023 s^{-1} and 0.78 A g^{-1}).[41] The OER performance of meso-$Mn_1Fe_1O_x$ is better than that of the best MnFe-based oxyhydroxides previously reported (Fig. 4c and Table S1†), for instance Mn–Fe oxide/CC (η_{10} = 730 mV),[42] $Mn_{0.5}Fe_{2.5}O_4$NP/MC (η_{10} = 560 mV),[43] $MnFe_2O_4$NP/MC (η_{10} = 510 mV),[43] Fe/Mn–N–C (η_{10} = 360 mV),[44] $Fe_{1.1}Mn_{0.9}P$ (η_{10} = 440 mV),[39] $MnFe_2O_4$/NF (η_{10} = 310 mV),[45] and $MnFe_2O_4$ (η_{10} = 582 mV),[46] and even exceeds that of the state-of-the-art RuO_2 catalyst (η_{10} = 340 mV).[47]

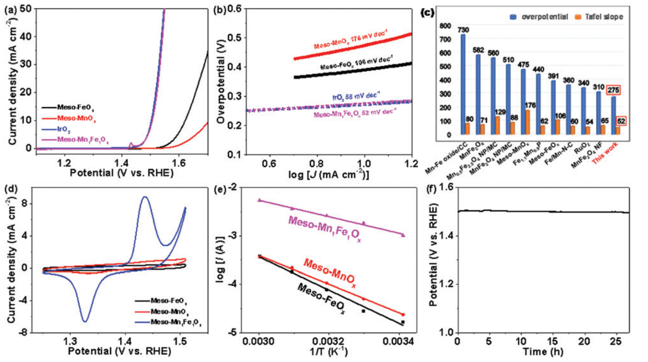

Fig. 4 (a) LSV curves of meso-FeO_x, meso-MnO_x, IrO_2, and meso-$Mn_1Fe_1O_x$. (b) Tafel slopes. (c) Comparison of overpotentials at 10 mA cm^{-2} and Tafel slopes. (d) CV curves at a scan rate of 100 mV s^{-1}. (e) Arrhenius plots. (f) Chronopotentiometric curve.

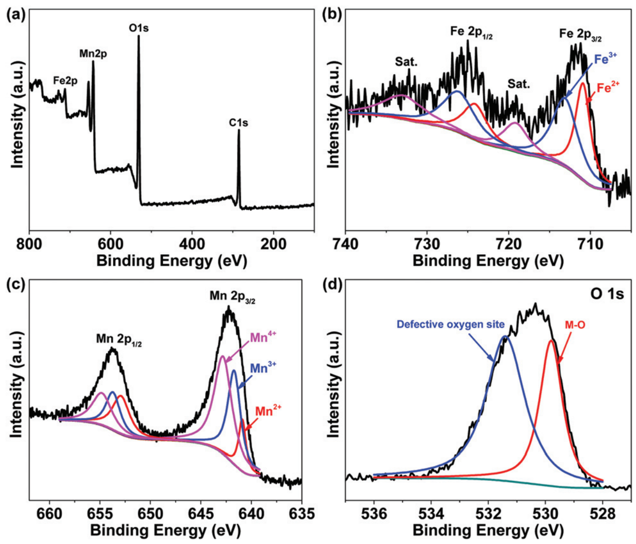

Fig. 3 (a) XPS survey spectrum of meso-$Mn_1Fe_1O_x$. (b) Fe 2p XPS spectrum. (c) Mn 2p XPS spectrum. (d) O 1s XPS spectrum.

The cyclic voltammogram (CV) of meso-FeO_x displays a very weak redox wave at $E_{1/2}$ = 1.396 V due to the one-electron redox reaction of the Fe^{2+}/Fe^{3+} couple (Fig. 4d), while the CV curve of meso-MnO_x exhibits a weak redox wave at $E_{1/2}$ = 1.392 V due to the one-electron redox reaction of the Mn^{3+}/Mn^{4+} couple.[25] The CV curve of meso-$Mn_1Fe_1O_x$ demonstrates a distinct redox wave at $E_{1/2}$ = 1.38 V (Fig. S8†), different from the monometallic Fe/Mn oxyhydroxides, implying a cooperative mechanism between Fe and Mn during OER electrocatalysis. The kinetic barrier on these catalysts can be derived from the Arrhenius formula $\left(E_a = -2.3R\frac{\partial \log(i_k)}{\partial \frac{1}{T}}\right)$, where i_k is the kinetic current at η = 300 mV, T is the temperature, and R is the universal gas constant (Fig. S9†).[48] meso-$Mn_1Fe_1O_x$ exhibits a low kinetic barrier of 32.7 kJ mol^{-1}, much smaller than meso-FeO_x (65.8 kJ mol^{-1}) and meso-MnO_x (56.7 kJ mol^{-1}) (Fig. 4e), indicating that a synergic action should be involved between Fe and Mn for accelerating the OER kinetics.

To assess the active sites in meso-FeO_x, meso-MnO_x, and meso-$Mn_1Fe_1O_x$, the electrochemically active surface area (ECSA) was compared (Fig. S10–S12†). meso-FeO_x shows an ECSA of 28.0 cm^2, which is close to that of meso-MnO_x (27.5 cm^2), but much lower than that of meso-$Mn_1Fe_{0.4}O_x$

(155.3 cm^2), meso-$Mn_1Fe_{0.6}O_x$ (184.2 cm^2), meso-$Mn_1Fe_{0.8}O_x$ (206.8 cm^2), meso-$Mn_1Fe_1O_x$ (405.0 cm^2), and meso-$Mn_{1.2}Fe_1O_x$ (142.1 cm^2), indicating that the efficient active sites can be greatly increased by the cooperation between Fe and Mn. Moreover, the charge-transfer ability of these catalysts was measured by electrochemical impedance spectroscopy (Fig. S13†). By fitting the Nyquist plots, the charge transfer resistance (R_{ct}) of meso-$Mn_1Fe_1O_x$ is only 3.6 Ω cm^2, much lower than that of meso-FeO_x (6.9 Ω cm^2), meso-MnO_x (6.8 Ω cm^2), meso-$Mn_1Fe_{0.4}O_x$ (4.8 Ω cm^2), meso-$Mn_1Fe_{0.6}O_x$ (4.6 Ω cm^2), meso-$Mn_1Fe_{0.8}O_x$ (4.2 Ω cm^2), and meso-$Mn_1Fe_{1.2}O_x$ (5.3 Ω cm^2). The fast charge-transfer ability of meso-$Mn_1Fe_1O_x$ facilitates OER kinetics in good agreement with the aforementioned results.

The OER durability of meso-$Mn_1Fe_1O_x$ was evaluated by chronopotentiometry measurement (Fig. 4f). After continuous operation at a constant current density of 10 mA cm^{-2} for 27 h, the potential remains constant, indicating excellent stability. The faradaic efficiency was found to be close to 100%, indicating that the anode current is from the OER. The structure of meso-$Mn_1Fe_1O_x$ after the OER test was analyzed by XRD (Fig. S14†), suggesting that the amorphous structure was retained after the stability test. The morphology and composition of meso-$Mn_1Fe_1O_x$ after the OER test were characterized by TEM, SEM, and EDS. As shown in Fig. S15,† mesopores can be still seen in the used meso-$Mn_1Fe_1O_x$. The morphology did not change obviously, and the Fe/Mn ratio was close to 1 : 1 as determined by EDS (Fig. S16†). The surface composition and metal valence state of meso-$Mn_1Fe_1O_x$ after the OER stability test were analyzed by XPS (Fig. S17†). Fe and Mn elements can be detected on the catalyst surface. The relative surface content of Fe^{3+}/Fe^{2+} increased from 1.2/1 in the initial sample to 1.5/1 in the used sample, while the Mn^{2+} in the initial sample was completely oxidized to a higher valence state (*i.e.* Mn^{4+}) after the OER, suggesting that Mn^{4+} is a key species for the OER.

Theoretical investigation

To rationally understand the excellent OER activity trend for meso-$Mn_1Fe_1O_x$, we theoretically probe the origin of OER activity enhancement by comparing the OER overpotentials (η^{OER}) of the unary γ-MnOOH (010) surface and binary Fe-doped γ-MnOOH (010) surfaces since γ-MnOOH is the most stable MnOOH polymorph which exhibited significant OER activity.[49] We first analyze three different monoatomic sites on pure and alloyed γ-MnOOH (010) surfaces. The free-energy diagrams (FEDs) of the OER are constructed for these monometallic sites and are shown in Fig. 5. The Fe site on the γ-MnOOH (010) surface is an uncoordinated site with 5 Mn–O coordination and it possesses a high η^{OER} of about 1.19 V, which can be attributed to the weak binding of *O and hence a large potential is required for *OH oxidation to *O (Fig. 5a). In addition, the OER activity for the Mn site cannot be improved when an Fe dopant occupies its neighboring site as shown in Fig. 5b. The surface Fe dopant is not the active site for the OER either because it binds all OER intermediates very weakly or its η^{OER} is 1.11 V due to the difficult *OH formation as can be seen in Fig. 5c.

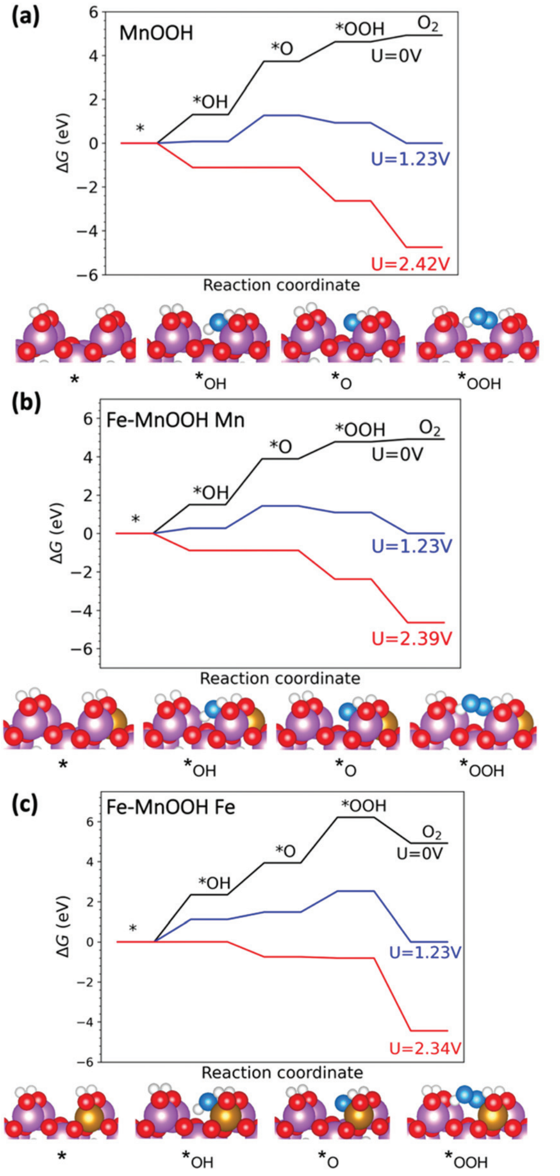

Fig. 5 Free-energy diagrams of the OER on different active sites: MnOOH (a), Fe-MnOOH Mn (b), and Fe-MnOOH Fe (c).

Since monometallic sites have poor OER activities owing to their weak binding of *O or *OH, we further examine the surface oxygen vacancy (O_v) sites and see if these sites have more balanced adsorption of OER intermediates. The surface O_v site coordinates to two metal ions. The FEDs of OER on these sites are shown in Fig. 6. On the pure γ-MnOOH (010) surface, the O_v site has an η^{OER} of 1.16 V (Fig. 6a), which is close to the above discussed monometallic Mn site on the pure γ-MnOOH (010) surface. However, the potential-determining step is now switched to the O–O coupling step due to enhanced *O adsorption and relatively weaker *OOH adsorption, *i.e.* a high value of $\Delta G^*_{OOH} - \Delta G^*_{O}$. The change of the potential-determining step indicates that the O_v site does modulate the binding of *O but

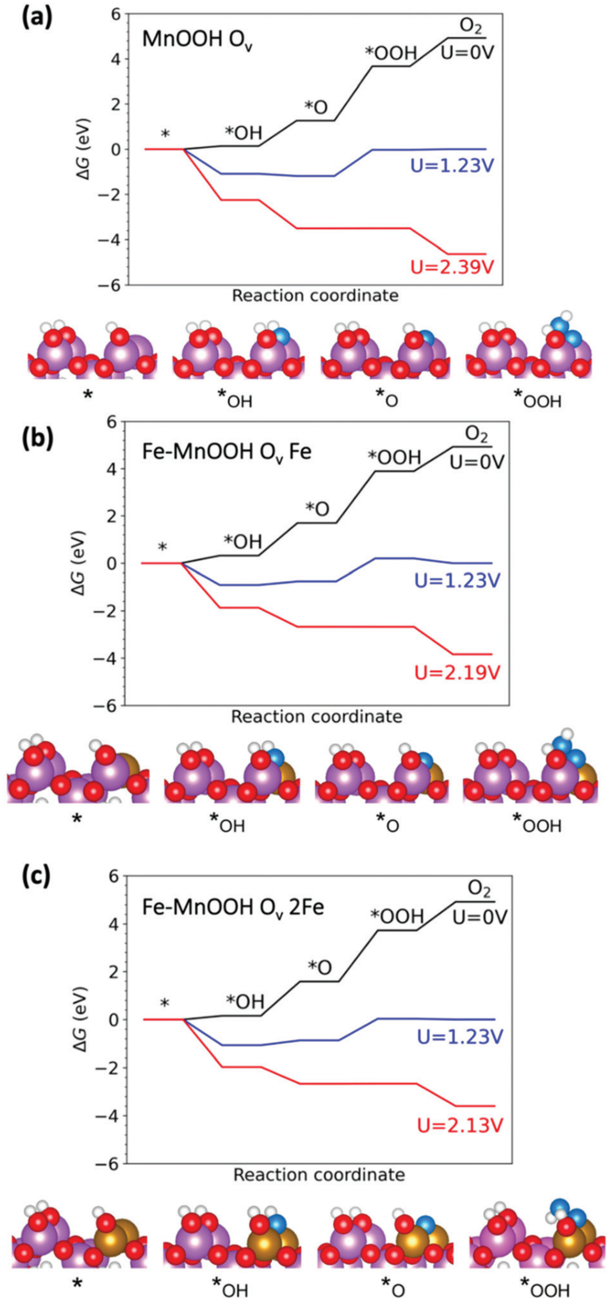

Fig. 6 Free energy diagrams of the OER on different active sites: MnOOH O_v (a), Fe-MnOOH O_v Fe (b), and Fe-MnOOH O_v 2Fe (c).

makes *O binding overly strong. For O_v sites that are in between mixed with the Mn and Fe ions, the strong *O binding can be alleviated and η^{OER} is reduced to 0.96 V as shown in Fig. 6b. The Fe–Fe O_v site has a similar η^{OER} as compared to the Mn–Fe O_v site as shown in Fig. 6c. Therefore, it is concluded that the surface doping of Fe can moderately destabilize the surface bridge O atoms on the γ-MnOOH (010) surface and facilitate the formation of surface oxygen vacancies that can serve as highly active sites for the OER.

Conclusions

In summary, a facile template method was adopted to synthesize mesoporous Mn–Fe oxyhydroxides with a high specific surface area and porous structure, which are advantageous to expose more actives for the OER. meso-$Mn_1Fe_1O_x$ exhibits efficient catalytic performance for the OER in alkaline media with a η_{10} of 275 mV, which surpasses most Mn-based electrocatalysts reported previously. Moreover, meso-$Mn_1Fe_1O_x$ is a durable OER electrocatalyst, which can retain its catalytic performance even after 27 h of long-term operation without any deactivation. Kinetic studies revealed that both Fe and Mn should synergistically catalyze the OER. DFT calculations confirmed that the MnOOH surface doped with Fe can favorably destabilize the surface bridge O atoms and accelerate the formation of surface oxygen vacancies, which are highly active for the OER.

Conflicts of interest

There are no conflicts to declare.

Acknowledgements

This work was supported by the National Natural Science Foundation of China (22075099) and the Education Department of Jilin Province (JJKH20220967KJ).

Notes and references

1 Q. Zhang and J. Guan, Applications of single-atom catalysts, *Nano Res.*, 2022, **15**, 38–70.
2 J. Guan, X. Bai and T. Tang, Recent progress and prospect of carbon-free single-site catalysts for the hydrogen and oxygen evolution reactions, *Nano Res.*, 2022, **15**, 818–837.
3 X. Wen, Q. Zhang and J. Guan, Applications of metal–organic framework-derived materials in fuel cells and metal-air batteries, *Coord. Chem. Rev.*, 2020, **409**, 213214.
4 Z. Chen, L. Guo, L. Pan, T. Yan, Z. He, Y. Li, C. Shi, Z.-F. Huang, X. Zhang and J.-J. Zou, Advances in oxygen evolution electrocatalysts for proton exchange membrane water electrolyzers, *Adv. Energy Mater.*, 2022, **12**, 2103670.
5 M. Tahir, L. Pan, F. Idrees, X. Zhang, L. Wang, J.-J. Zou and Z. L. Wang, Electrocatalytic oxygen evolution reaction for energy conversion and storage: A comprehensive review, *Nano Energy*, 2017, **37**, 136–157.
6 Q. Zhang and J. Guan, Applications of atomically dispersed oxygen reduction catalysts in fuel cells and zinc-air batteries, *Energy Environ. Mater.*, 2021, **4**, 307–335.
7 Y. Li, Y. Sun, Y. Qin, W. Zhang, L. Wang, M. Luo, H. Yang and S. Guo, Recent advances on water-splitting electrocatalysis mediated by noble-metal-based nanostructured materials, *Adv. Energy Mater.*, 2020, **10**, 1903120.

8 Z. Lei, T. Wang, B. Zhao, W. Cai, Y. Liu, S. Jiao, Q. Li, R. Cao and M. Liu, Recent progress in electrocatalysts for acidic water oxidation, *Adv. Energy Mater.*, 2020, **10**, 2000478.

9 M. Wang, L. Zhang, Y. He and H. Zhu, Recent advances in transition-metal-sulfide-based bifunctional electrocatalysts for overall water splitting, *J. Mater. Chem. A*, 2021, **9**, 5320–5363.

10 X. Xia, L. Wang, N. Sui, V. L. Colvin and W. W. Yu, Recent progress in transition metal selenide electrocatalysts for water splitting, *Nanoscale*, 2020, **12**, 12249–12262.

11 X. Zhao, X. Kong, Z. Liu, Z. Li, Z. Xie, Z. Wu, F. He, X. Chang, P. Yang, J. Zheng and X. Li, The cutting-edge phosphorus-rich metal phosphides for energy storage and conversion, *Nano Today*, 2021, **40**, 101245.

12 Y. Jiang and Y. Lu, Designing transition-metal-boride-based electrocatalysts for applications in electrochemical water splitting, *Nanoscale*, 2020, **12**, 9327–9351.

13 H. Wang, S. Zhu, J. Deng, W. Zhang, Y. Feng and J. Ma, Transition metal carbides in electrocatalytic oxygen evolution reaction, *Chin. Chem. Lett.*, 2021, **32**, 291–298.

14 D. Tian, S. R. Denny, K. Li, H. Wang, S. Kattel and J. G. Chen, Density functional theory studies of transition metal carbides and nitrides as electrocatalysts, *Chem. Soc. Rev.*, 2021, **50**, 12338–12376.

15 F. Song, L. Bai, A. Moysiadou, S. Lee, C. Hu, L. Liardet and X. Hu, Transition Metal Oxides as Electrocatalysts for the Oxygen Evolution Reaction in Alkaline Solutions: An Application-Inspired Renaissance, *J. Am. Chem. Soc.*, 2018, **140**, 7748–7759.

16 Q. Zhang and J. Guan, Atomically dispersed catalysts for hydrogen/oxygen evolution reactions and overall water splitting, *J. Power Sources*, 2020, **471**, 228446.

17 C. Feng, M. B. Faheem, J. Fu, Y. Xiao, C. Li and Y. Li, Fe-Based Electrocatalysts for Oxygen Evolution Reaction: Progress and Perspectives, *ACS Catal.*, 2020, **10**, 4019–4047.

18 B. M. Hunter, H. B. Gray and A. M. Müller, Earth-Abundant Heterogeneous Water Oxidation Catalysts, *Chem. Rev.*, 2016, **116**, 14120–14136.

19 Y. Qian, X. Xu, Y. He, L. Lei, Y. Xia and X. Zhang, A novel monoclinic metal oxide catalyst for oxygen evolution reactions in alkaline media, *Inorg. Chem. Front.*, 2022, **9**, 941–949.

20 B. Zhang, Y. Li, M. Valvo, L. Fan, Q. Daniel, P. Zhang, L. Wang and L. Sun, Electrocatalytic Water Oxidation Promoted by 3D Nanoarchitectured Turbostratic delta-MnOx on Carbon Nanotubes, *ChemSusChem*, 2017, **10**, 4472–4478.

21 H. Wang, K. H. L. Zhang, J. P. Hofmann, V. A. de la Pena O'Shea and F. E. Oropeza, The electronic structure of transition metal oxides for oxygen evolution reaction, *J. Mater. Chem. A*, 2021, **9**, 19465–19488.

22 L.-H. Liu, N. Li, M. Han, J.-R. Han and H.-Y. Liang, Scalable synthesis of nanoporous high entropy alloys for electrocatalytic oxygen evolution, *Rare Met.*, 2022, **41**, 125–131.

23 X. Bai, L. Wang, B. Nan, T. Tang, X. Niu and J. Guan, Atomic manganese coordinated to nitrogen and sulfur for oxygen evolution, *Nano Res.*, 2022, DOI: **10.1007/s12274-022-4293-7**.

24 M. Shamsipur and A. Pashabadi, Latest advances in PSII features and mechanism of water oxidation, *Coord. Chem. Rev.*, 2018, **374**, 153–172.

25 J. Guan, Z. Duan, F. Zhang, S. D. Kelly, R. Si, M. Dupuis, Q. Huang, J. Q. Chen, C. Tang and C. Li, Water oxidation on a mononuclear manganese heterogeneous catalyst, *Natl. Catal.*, 2018, **1**, 870–877.

26 A. Li, H. Ooka, N. Bonnet, T. Hayashi, Y. Sun, Q. Jiang, C. Li, H. Han and R. Nakamura, Stable Potential Windows for Long-Term Electrocatalysis by Manganese Oxides Under Acidic Conditions, *Angew. Chem., Int. Ed.*, 2019, **58**, 5054–5058.

27 A. Ramirez, P. Hillebrand, D. Stellmach, M. M. May, P. Bogdanoff and S. Fiechter, Evaluation of MnOx, Mn2O3, and Mn3O4 Electrodeposited Films for the Oxygen Evolution Reaction of Water, *J. Phys. Chem. C*, 2014, **118**, 14073–14081.

28 M. Huynh, C. Shi, S. J. L. Billinge and D. G. Nocera, Nature of Activated Manganese Oxide for Oxygen Evolution, *J. Am. Chem. Soc.*, 2015, **137**, 14887–14904.

29 S. Sun, G. Shen, J. Jiang, W. Mi, X. Liu, L. Pan, X. Zhang and J.-J. Zou, Boosting oxygen evolution kinetics by Mn–N–C motifs with tunable spin state for highly efficient solar-driven water splitting, *Adv. Energy Mater.*, 2019, **9**, 1901505.

30 P. Yan, Q. Liu, H. Zhang, L. Qiu, H. B. Wu and X.-Y. Yu, Deeply reconstructed hierarchical and defective NiOOH/FeOOH nanoboxes with accelerated kinetics for the oxygen evolution reaction, *J. Mater. Chem. A*, 2021, **9**, 15586–15594.

31 S. Anantharaj, S. Kundu and S. Noda, "The Fe Effect": A review unveiling the critical roles of Fe in enhancing OER activity of Ni and Co based catalysts, *Nano Energy*, 2021, **80**, 105514.

32 G. Shen, R. Zhang, L. Pan, F. Hou, Y. Zhao, Z. Shen, W. Mi, C. Shi, Q. Wang, X. Zhang and J.-J. Zou, Regulating the spin state of FeIII by atomically anchoring on ultrathin titanium dioxide for efficient oxygen evolution electrocatalysis, *Angew. Chem., Int. Ed.*, 2020, **59**, 2313–2317.

33 Q. Ma, R. Dong, H. Liu, A. Zhu, L. Qiao, Y. Ma, J. Wang, J. Xie and J. Pan, Prussian blue analogue-derived Mn-Fe oxide nanocubes with controllable crystal structure and crystallinity as highly efficient OER electrocatalysts, *J. Alloys Compd.*, 2020, **820**, 153438.

34 Y. Teng, X.-D. Wang, J.-F. Liao, W.-G. Li, H.-Y. Chen, Y.-J. Dong and D.-B. Kuang, Atomically Thin Defect-Rich Fe-Mn-O Hybrid Nanosheets as High Efficient Electrocatalyst for Water Oxidation, *Adv. Funct. Mater.*, 2018, **28**, 1802463.

35 J. Luo, W. H. Guo, Q. Zhang, X. H. Wang, L. Shen, H. C. Fu, L. L. Wu, X. H. Chen, H. Q. Luo and N. B. Li, One-pot synthesis of Mn-Fe bimetallic oxide heterostructures as bifunctional electrodes for efficient overall water splitting, *Nanoscale*, 2020, **12**, 19992–20001.

36 K. Lemoine, Z. Gohari-Bajestani, R. Moury, A. Terry, A. Guiet, J.-M. Greneche, A. Hemon-Ribaud, N. Heidary, V. Maisonneuve, N. Kornienko and J. Lhoste, Amorphous Iron-Manganese Oxyfluorides, Promising Catalysts for Oxygen Evolution Reaction under Acidic Media, *ACS Appl. Energy Mater.*, 2021, **4**, 1173–1181.

37 R. Subbaraman, D. Tripkovic, K.-C. Chang, D. Strmcnik, A. P. Paulikas, P. Hirunsit, M. Chan, J. Greeley, V. Stamenkovic and N. M. Markovic, Trends in activity for the water electrolyser reactions on 3d M(Ni,Co,Fe,Mn) hydr (oxy)oxide catalysts, *Nat. Mater.*, 2012, **11**, 550–557.

38 H.-l. Wei, A.-d. Tan, S.-z. Hu, J.-h. Piao and Z.-y. Fu, Efficient spinel iron-cobalt oxide/nitrogen-doped ordered mesoporous carbon catalyst for rechargeable zinc-air batteries, *Chin. J. Catal.*, 2021, **42**, 1451–1458.

39 R. Liu, Y. Wang, D. Liu, Y. Zou and S. Wang, Water-Plasma-Enabled Exfoliation of Ultrathin Layered Double Hydroxide Nanosheets with Multivacancies for Water Oxidation, *Adv. Mater.*, 2017, **29**, 1701546.

40 C. Dong, X. Yuan, X. Wang, X. Liu, W. Dong, R. Wang, Y. Duan and F. Huang, Rational design of cobalt-chromium layered double hydroxide as a highly efficient electrocatalyst for water oxidation, *J. Mater. Chem. A*, 2016, **4**, 11292–11298.

41 B. Zhang, X. Zheng, O. Voznyy, R. Comin, M. Bajdich, M. García-Melchor, L. Han, J. Xu, M. Liu, L. Zheng, F. P. García de Arquer, C. T. Dinh, F. Fan, M. Yuan, E. Yassitepe, N. Chen, T. Regier, P. Liu, Y. Li, P. De Luna, A. Janmohamed, H. L. Xin, H. Yang, A. Vojvodic and E. H. Sargent, Homogeneously dispersed multimetal oxygen-evolving catalysts, *Science*, 2016, **352**, 333–337.

42 N. Bhandary, P. P. Ingole and S. Basu, Electrosynthesis of Mn-Fe oxide nanopetals on carbon paper as bi-functional electrocatalyst for oxygen reduction and oxygen evolution reaction, *Int. J. Hydrogen Energy*, 2018, **43**, 3165–3171.

43 Y. Konno, T. Yamamoto and T. Nagayama, Nanoporous manganese ferrite films by anodising electroplated Fe-Mn alloys for bifunctional oxygen electrodes, *Nanoscale*, 2021, **13**, 12738–12749.

44 X. Wu, Y. Niu, B. Feng, Y. Yu, X. Huang, C. Zhong, W. Hu and C. M. Li, Mesoporous Hollow Nitrogen-Doped Carbon Nanospheres with Embedded MnFe2O4/Fe Hybrid Nanoparticles as Efficient Bifunctional Oxygen Electrocatalysts in Alkaline Media, *ACS Appl. Mater. Interfaces*, 2018, **10**, 20440–20447.

45 M. Li, Y. Xiong, X. Liu, X. Bo, Y. Zhang, C. Han and L. Guo, Facile synthesis of electrospun MFe2O4 (M = Co, Ni, Cu, Mn) spinel nanofibers with excellent electrocatalytic properties for oxygen evolution and hydrogen peroxide reduction, *Nanoscale*, 2015, **7**, 8920–8930.

46 C. Si, Y. Zhang, C. Zhang, H. Gao, W. Ma, L. Lv and Z. Zhang, Mesoporous nanostructured spinel-type MFe2O4 (M = Co, Mn, Ni) oxides as efficient bi-functional electrocatalysts towards oxygen reduction and oxygen evolution, *Electrochim. Acta*, 2017, **245**, 829–838.

47 Y. Lee, J. Suntivich, K. J. May, E. E. Perry and Y. Shao-Horn, Synthesis and Activities of Rutile IrO2 and RuO2 Nanoparticles for Oxygen Evolution in Acid and Alkaline Solutions, *J. Phys. Chem. Lett.*, 2012, **3**, 399–404.

48 J. R. Swierk, S. Klaus, L. Trotochaud, A. T. Bell and T. D. Tilley, Electrochemical Study of the Energetics of the Oxygen Evolution Reaction at Nickel Iron (Oxy)Hydroxide Catalysts, *J. Phys. Chem. C*, 2015, **119**, 19022–19029.

49 P. F. Smith, B. J. Deibert, S. Kaushik, G. Gardner, S. Hwang, H. Wang, J. F. Al-Sharab, E. Garfunkel, L. Fabris, J. Li and G. C. Dismukes, Coordination Geometry and Oxidation State Requirements of Corner-Sharing MnO6 Octahedra for Water Oxidation Catalysis: An Investigation of Manganite (γ-MnOOH), *ACS Catal.*, 2016, **6**, 2089–2099.